Supplementary Material: Optical absorption spectra of metal oxides from time-dependent density functional theory and many-body perturbation theory based on optimally-tuned hybrid functionals

Guy Ohad,[1] Stephen E. Gant,[2,3] Dahvyd Wing,[1] Jonah B. Haber,[2,3] María Camarasa-Gómez,[1] Francisca Sagredo,[2,3] Marina R. Filip,[4] Jeffrey B. Neaton,[2,3,5] and Leeor Kronik[1]

[1]*Department of Molecular Chemistry and Materials Science, Weizmann Institute of Science, Rehovoth 76100, Israel*
[2]*Department of Physics, University of California, Berkeley, CA 94720*
[3]*Materials Sciences Division, Lawrence Berkeley National Laboratory, Berkeley, CA 94720*
[4]*Department of Physics, University of Oxford, Oxford OX1 3PJ, United Kingdom*
[5]*Kavli Energy NanoSciences Institute at Berkeley, University of California, Berkeley, CA 94720*

S.I. COMPUTATIONAL DETAILS FOR THE (TD)DFT CALCULATIONS

All calculations are performed with the Vienna *ab initio* simulation package (VASP) [1]. We use the PBE-based projector augmented wave (PAW) method for treating core electrons [2]. The PAW for O that is used throughout includes the $2s$ and $2p$ electrons. For the other elements, different PAWs are required to converge the calculated property. Below we elaborate which ones are used for each step in the WOT-SRSH procedure. Spin-orbit coupling effects are neglected throughout.

Steps 1 and 4: Dielectric constant and quasiparticle band gap calculations. We calculate the average of the trace of the ion-clamped dielectric tensor, ε_∞, from the change in polarization in response to a finite electric field, including local field effects in both the Hartree and exchange-correlation potentials. The energy cutoff used is 500 eV. The $\boldsymbol{k}$-grid and metal PAWs are reported in Table S.I.

Steps 2 and 3: Wannierization and tuning. We use supercells evaluated with a Γ-point-only sampling of the Brillouin zone. We enforce the occupation of the Wannier function to be less than 1×10^{-4} by setting $\lambda = 300$ eV. To correct the energy of the $N-1$-electron system we use one of two image charge corrections. The first one is the isotropic Makov-Payne monopole image charge correction [3–5], where the supercell length is taken as the cubic root of the volume of the supercell, and ε_∞ is taken from step 1. The second one is more accurate for incorporating anisotropy [6] and is used only for the case of Al_2O_3. The maximally localized Wannier functions in step 2 are generated using the WANNIER90 software package [7]. To generate the supercell, for MgO and CaO we use the cubic unit-cell, for Al_2O_3 we use the hexagonal unit cell and for $BiVO_4$ we use a pseudo-orthorhombic unit cell obtained from doubling the primitive unit cell. For all other materials we use the primitive unit cell to generate the supercell. The PAWs used are the same ones reported in Table S.I. One exception is for V where we use the $3d4s$ configuration, as it is more stable in converging the self-consistent cycle in supercell calculations. The plane wave cutoff energies and supercell sizes are reported in Table S.II.

TDDFT calculations. For Al_2O_3 we use the rhombohedral unit cell. We use the same PAWs reported in Table S.I, except for the case of $BiVO_4$ where we use Bi: $6s6p$ and V: $3d4s$. This is because these simpler PAWs converge the spectra to a similar level of accuracy relative to the more advanced PAWs (within ∼0.1 eV) while being more computationally efficient especially for large $\boldsymbol{k}$-grid calculations. A Lorentzian broadening is used to interpret the spectra. The convergence of the TDDFT spectra with respect to the $\boldsymbol{k}$-grid for selected materials is demonstrated in Fig. S.I. Further details are given in Table S.III.

The $\boldsymbol{k}$-shifts in Table S.III were chosen according to the heuristic approach suggested in Ref. [8]. For each material, we generate a list of $n_1 \times n_2 \times n_3$ different $\boldsymbol{k}$-shifts, while taking into account the symmetry of the crystal in order to remove equivalent $\boldsymbol{k}$-shifts from the list, such that we obtain $N_{k-\text{shift}}$ unique $\boldsymbol{k}$-shifts (see Table S.IV). We then generate $N_{k-\text{shift}}$ $\boldsymbol{k}$-grids of size $10 \times 10 \times 10$ (except for $BiVO_4$ where we use $6 \times 6 \times 9$), each shifted by a different amount, and perform a DFT calculation at the PBE level for each shifted grid. Next, we compute the variance of the spacing in energy between band gaps in the $\boldsymbol{k}$-grid. Finally, we select the $\boldsymbol{k}$-shift leading to the smallest variance. The plane wave cutoff energy, PAWs and unit cells used for these calculations are the same ones as in the TDDFT calculations.

TABLE S.I: $\boldsymbol{k}$-grid and metal PAWs used in dielectric constant and quasiparticle band gap calculations.

	$\boldsymbol{k}$-grid	Metal PAW
MgO	$6 \times 6 \times 6$	$2s^2 2p^6 3s^2$
Al_2O_3	$5 \times 5 \times 2$[a]	$3s^2 3p^1$
CaO	$4 \times 4 \times 4$	$3s^2 3p^6 4s^2$
TiO_2	$4 \times 4 \times 6$	$3s^2 3p^6 3d^2 4s^2$
Cu_2O	$4 \times 4 \times 4$	$3d^{10} 4s^1$
ZnO	$5 \times 5 \times 3$	$3d^{10} 4s^2$
$BaSnO_3$	$4 \times 4 \times 4$	Ba: $5s^2 5p^6 6s^2$, Sn: $4d^{10} 5s^2 5p^2$
$BiVO_4$	$4 \times 4 \times 6$	Bi: $5d^{10} 6s^2 6p^3$, V: $3p^6 3d^3 4s^2$

[a]Using the hexagonal unit cell

TABLE S.II: Plane wave cutoff energies and supercell sizes used in the Wannierization and tuning calculatiuons.

	E_{cutoff} (eV)	Supercell size
MgO	600	$2 \times 2 \times 2$
Al_2O_3	600	$2 \times 2 \times 1$
CaO	500	$2 \times 2 \times 2$
TiO_2	400	$2 \times 2 \times 3$
Cu_2O	400	$2 \times 2 \times 2$
ZnO	500	$3 \times 3 \times 2$
$BaSnO_3$	400	$2 \times 2 \times 2$
$BiVO_4$	400	$2 \times 2 \times 1$

TABLE S.III: Computational parameters for TDDFT calculations. N_v and N_c are the number of valence bands and conduction bands, respectively, in the vicinity of the Fermi level, that are used in the evaluation of the kernel.

	E_{cutoff} (eV)	$\boldsymbol{k}$-grid	$\boldsymbol{k}$-shift	N_v	N_c	Broadening (eV)
MgO	600	$14 \times 14 \times 14$	$0.0500 \times 0.3000 \times 0.5500$	7	13	0.10
Al_2O_3	400	$6 \times 6 \times 6$[a]	$0.3125 \times 0.3750 \times 0.5625$	18	24	0.20
CaO	600	$14 \times 14 \times 14$	$0.0500 \times 0.2000 \times 0.7000$	7	13	0.10
TiO_2	400	$7 \times 7 \times 10$	$0.0625 \times 0.3750 \times 0.4375$	12	12	0.10
Cu_2O	400	$10 \times 10 \times 10$	$0.2000 \times 0.3000 \times 0.4500$	12	6	0.10
ZnO	500	$12 \times 12 \times 8$	$0.1000 \times 0.4000 \times 0.1667$	6	6	0.15
$BaSnO_3$	400	$8 \times 8 \times 8$	$0.1500 \times 0.3500 \times 0.4000$	15	28	0.25
$BiVO_4$	400	$8 \times 8 \times 11$	$0.2500 \times 0.0000 \times 0.2500$	22	16	0.10

[a]Using the rhombohedral unit cell

TABLE S.IV: The grid size used to generate the list of $\boldsymbol{k}$-shifts and the number of different $\boldsymbol{k}$-shifts obtained as a result, after taking into account the crystal symmetry.

	$n_1 \times n_2 \times n_3$	$N_{k-\text{shift}}$
MgO	$20 \times 20 \times 20$	256
Al_2O_3	$16 \times 16 \times 16$	417
CaO	$20 \times 20 \times 20$	256
TiO_2	$16 \times 16 \times 16$	405
Cu_2O	$20 \times 20 \times 20$	286
ZnO	$20 \times 20 \times 12$	528
$BaSnO_3$	$20 \times 20 \times 20$	286
$BiVO_4$	$8 \times 8 \times 12$	768

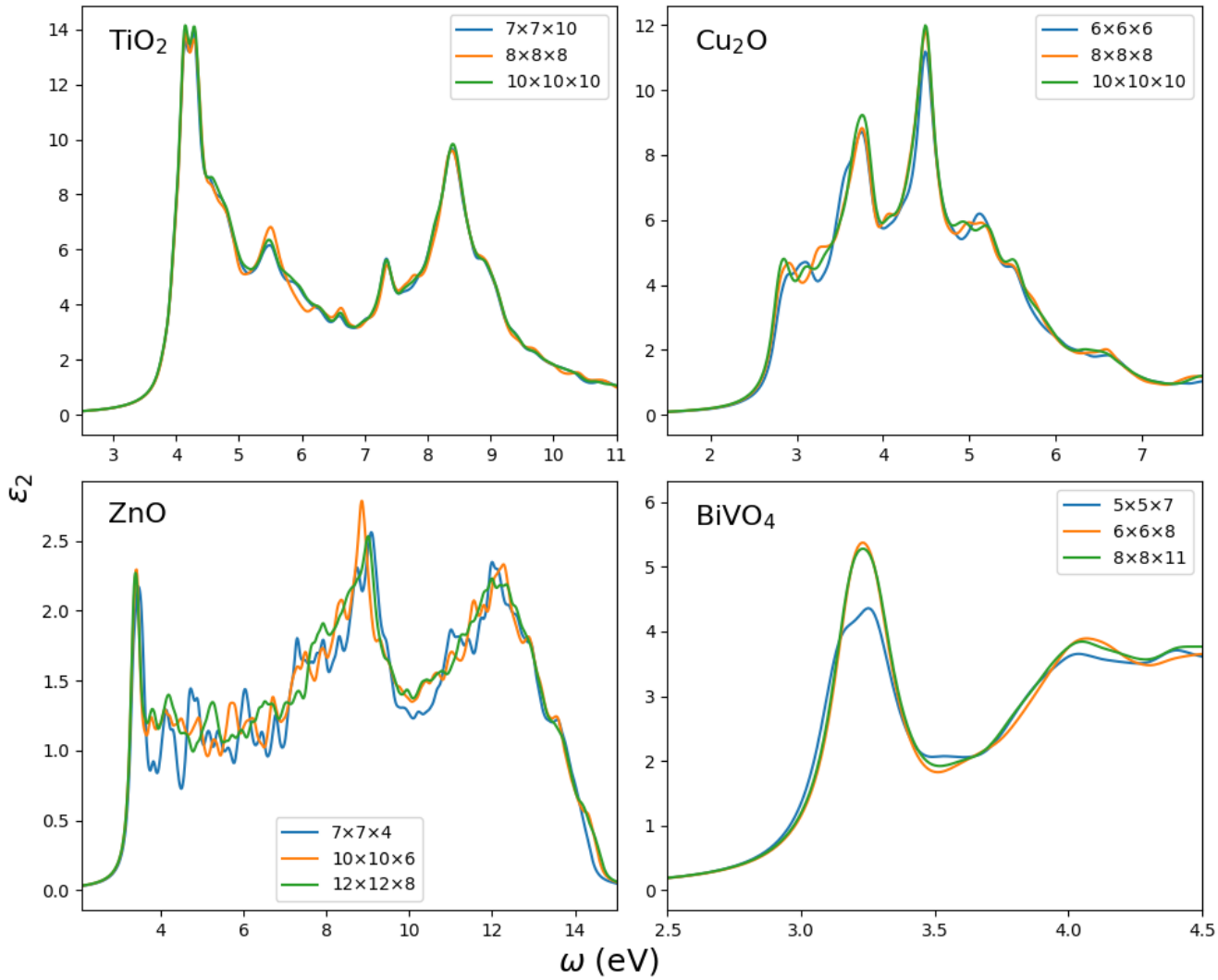

FIG. S.I: Convergence of TDDFT optical absorption spectra for different $\boldsymbol{k}$-grids, in the cases of TiO_2, Cu_2O, ZnO and $BiVO_4$. The optical response is directionally averaged in all spectra. Vibrational renormalization is not included.

S.II. COMPUTATIONAL DETAILS FOR THE *GW*-BSE CALCULATIONS

The staring-point DFT eigensystems for our *GW*-BSE calculations are computed using a modified version of the QUANTUM ESPRESSO plane-wave code [9–11] that allows for the use of the SRSH functional, and our *GW*-BSE calculations are carried out using the BerkeleyGW software package [12]. We use optimized norm-conserving fully-relativistic Vanderbilt pseudopotentials [13] obtained from the online repository, pseudo-dojo [14]. For the elements Mg, Ca, Ti, Cu, Zn, Ba, Sn, Bi, and V, we explicitly include a full shell of semicore electrons, because the explicit consideration of deeper states has been shown to be necessary for an accurate description of the electronic structure when carrying out *GW* as well as DFT hybrid functional calculations [15–18]. For all systems except Cu_2O, the frequency dependence of the screened Coulomb interaction is handled explicitly through a full-frequency contour deformation (FF-CD) approach using the Adler-Wiser formula [19, 20]. For each system, 20 frequencies are sampled from the imaginary axis, while the real axis was sampled on a grid as specified in Table S.V. In order to reduce computational cost, the frequency-dependent part of the polarizability is expanded in the basis formed by the leading eigenvectors of the static polarizability via the static subspace approximation [21]. In this approximation, the eigenvalue cutoff is set to 0.001, which has been shown to maintain a high level of precision [21]. For Cu_2O, numerical instability is encountered when solving for the self-energy using the FF-CD method. As such, the frequency dependence of the polarizability is modeled using the Godby-Needs generalized plasmon pole model (GN-GPPM) [22, 23], which has been shown to closely replicate full-frequency results [24]. Full details on the input parameters used to calculate the screening matrix, including the cutoff employed for the screened interaction, as well as the $\boldsymbol{k}$-grid used to construct it, can be found in Table S.V.

The self-energy $\Sigma \approx G_0W_0$ and dielectric function ε are constructed using 1024 bands for each system. This choice is a compromise between computational tractability/parallelization and accuracy, and while it generally produced enough unoccupied states to yield a well-converged ε, the self-energy is slightly under-converged for some of the more demanding compounds under study. In order to gauge the level of convergence, we perform two independent fits using G_0W_0@PBE results for the direct band gap at Γ. The first is

$$E_g^\Gamma = \left(a_1 + a_2\frac{1}{N_G}\right)\left(b_1 + b_2\frac{1}{N_b^{(\varepsilon)}}\right)\left(c_1 + c_2\frac{1}{N_b^{(\Sigma)}}\right), \tag{1}$$

where N_G is the number of $\boldsymbol{G}$ vectors used to constructed ε as dictated by the choice of screened interaction cutoff and $N_b^{(\varepsilon)}$, $N_b^{(\Sigma)}$ are the numbers of bands used to construct ε and Σ respectively [21]. The second fit is simply

$$E_g^\Gamma = d_1 + d_2\frac{1}{N_q}, \tag{2}$$

where N_q is the number of $\boldsymbol{q}$ points used to construct ε. Using these fits, we estimate the convergence error in E_g^Γ for the choice of convergence parameters, see Table S.V.

The static remainder approximation (SRA) to the self-energy [25] is employed only for Cu_2O. In general, we find that the use of the SRA did not impact the rate of convergence when using GN-GPPM or FF-CD dielectric functions, though it did tend to change the direction from which convergence was approached (from below without and from above with, for E_g^Γ). However, in the case of Cu_2O, it is necessary to employ the SRA in order to prevent an erroneous conduction band reordering. This convergence issue has been documented to occur for *GW* calculations performed on GGA functionals and was resolved in prior work via the usage of an on-site potential [26, 27].

TABLE S.V: Convergence parameters of the G_0W_0@WOT-SRSH calculations.

	$\boldsymbol{k}$-grid	ε Cutoff (Ry)	$N_b^{(\Sigma,\varepsilon)}$	ω Dependence Method	Δ_ω (eV)	ω_{cut} (eV)	Extrap. E_g^Γ Error (eV)
MgO	6x6x6	80	1024	FF-CD	0.15	15	−0.03
Al_2O_3	3x3x3	30	1024	FF-CD	0.25	25	−0.12
CaO	6x6x6	50	1024	FF-CD	0.1	15	−0.08
TiO_2	3x3x5	50	1024	FF-CD	0.15	10	0.02
Cu_2O	4x4x4	80	1024	GN-GPPM			0.01
ZnO	7x7x4	80	1024	FF-CD	0.2	20	−0.08
$BaSnO_3$	6x6x6	70	1024	FF-CD	0.15	15	−0.03
$BiVO_4$	3x3x4	40	1024	FF-CD	0.15	15	0.01

The parameters used for BSE optical spectra are chosen to match those used in the TDDFT calculations as closely as possible. Thus, the number of occupied and unoccupied states and the size and shift of the fine $\boldsymbol{k}$-grid used in solving the BSE and Casida equation are the same (see Table S.III). In order to save computational cost, the BSE

kernel and G_0W_0 eigenvalues are interpolated from the coarse grids specified in Table S.V to the fine grids in Table S.III. In order to perform this interpolation it is often necessary to construct the BSE kernel on the coarse grid with more states than were used in the fine grid; these values can also be found in Table S.VI.

TABLE S.VI: Additional computational parameters regarding eigenvalue and kernel interpolation for BSE calculations. N_v and N_c are the number of valence bands and conduction bands used, with the fi or co superscripts denoting a $\boldsymbol{k}$-grid that is fine or coarse, respectively.

	N_v^{co}	N_c^{co}	N_v^{fi}	N_c^{fi}
MgO	7	17	7	13
Al_2O_3	18	28	18	24
CaO	7	17	7	13
TiO_2	12	15	12	12
Cu_2O	17	10	12	6
ZnO	10	8	6	6
$BaSnO_3$	18	40	15	28
$BiVO_4$	26	20	22	16

To further explore the impact of different DFT starting points we perform G_0W_0-BSE calculations for MgO using PBE and WOT-SRSH, as well as the local-density approximation (LDA) [28], HSE06, and PBE0 starting points in Fig. S.II. To reduce computational cost we lowered the ε cutoff used from 80 to 50 Ry, changed $N_b^{(\Sigma,\varepsilon)}$ from 1024 to 640, and employed the GN-GPPM, as opposed to FF-CD, for handling the frequency dependence. Additionally, we use scalar relativistic pseudopotentials. We do not expect these changes to result in more than a 0.1 eV shift in the spectra.

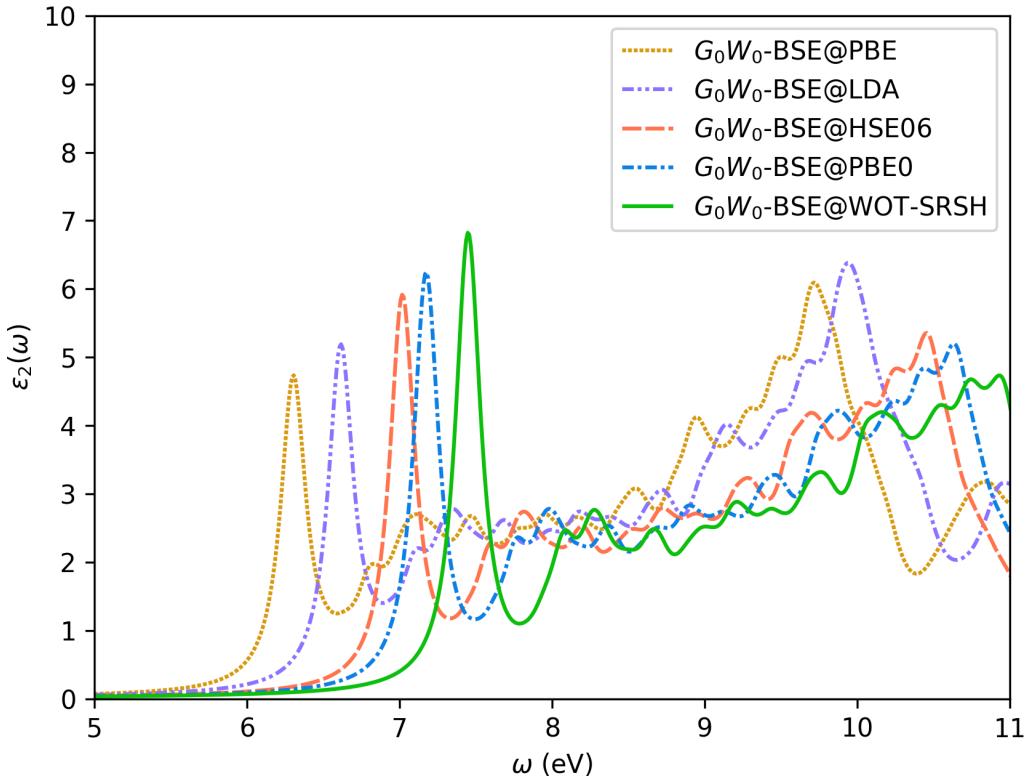

FIG. S.II: Optical absorption spectra of MgO calculated using G_0W_0-BSE for a variety of DFT starting point eigensystems. As in the main text, these spectra are red-shifted by -0.533 eV to account for the renormalization effect of lattice vibrations.

S.III. DIELECTRIC CONSTANT VALUES

TABLE S.VII: Values of the dielectric constant, ε_∞, used in WOT-SRSH (calculated including local field, LF, effects), and in the G_0W_0 calculations (calculated within the RPA).

	WOT-SRSH (LF)	PBE (RPA)	WOT-SRSH (RPA)
MgO	2.85	3.04	2.42
Al_2O_3	2.94	3.05	2.48
CaO	3.25	3.57	2.73
TiO_2	6.25	8.57	5.84
Cu_2O	6.51	11.00	4.77
ZnO	3.57	5.63	2.97
$BaSnO_3$	3.92	4.65	3.38
$BiVO_4$	5.92	6.99	5.36

S.IV. PHONON SCREENING CORRECTIONS TO THE EXCITON BINDING ENERGY

Ref. [29] derives an expression for the phonon screening correction to the $1s$ exciton binding energy at 0 K in the case of a single Fröhlich-coupled zone-center phonon, i.e.

$$\Delta E_B = -2\omega_{\mathrm{LO}} \left(1 - \frac{\varepsilon_\infty}{\varepsilon_0}\right) \frac{\sqrt{1+\omega_{\mathrm{LO}}/E_B}+3}{(1+\sqrt{1+\omega_{\mathrm{LO}}/E_B})^3}, \tag{3}$$

where ω_{LO} is the longitudinal-optical phonon frequency, ε_0 is the static dielectric constant and E_B is the exciton binding energy. Using this limit, we estimate the phonon screening correction to the exciton binding energy for the materials in this work. Using the WOT-SRSH functional, our estimates using this formula are given in Table S.VIII. The exciton binding energy is calculated as the difference between the smallest QP direct band gap and the onset of absorption. ω_{LO}, ε_∞, and ε_0 are calculated with the same numerical parameters used for the calculations in step 1, described in section S.I, except for the ionic contribution to ε_0 for TiO_2, calculated with a Ti PAW of configuration $3d4s$, owing to improved numerical stability.

TABLE S.VIII: Calculated quantities for use with Eq. (3) and the resulting approximate phonon screening corrections to the exciton binding energy.

	ω_{LO} [meV]	ε_∞	ε_0	E_B [meV]	ΔE_B [meV]
MgO	48	2.85	10.08	483	-32
Al_2O_3	107	2.94	10.11	472	-67
CaO	35	3.24	17.85	562	-27
TiO_2	101	6.23	176.57	87	-58
Cu_2O	81	6.51	7.37	156	-7
ZnO	65	3.57	8.10	282	-32
$BaSnO_3$	79	3.92	16.47	174	-47
$BiVO_4$	108	5.93	61.43	439	-85

S.V. FUNDAMENTAL BAND GAPS

TABLE S.IX: Quasiparticle fundamental band gaps, in eV, as computed here for all studied systems. Corrected values are obtained by adding the vibrational renormalization reported in the main text.

	WOT-SRSH	G_0W_0@WOT-SRSH	Corrected WOT-SRSH	Corrected G_0W_0@WOT-SRSH
MgO	8.3	8.7	7.7	8.2
Al_2O_3	9.8	10.4	9.5	10.1
CaO	6.6	7.2	6.3	6.9
TiO_2	3.5	3.7	3.2	3.5
Cu_2O	2.0	2.0	1.8	1.8
ZnO	3.5	3.5	3.3	3.3
$BaSnO_3$	3.5	3.7	3.1	3.3
$BiVO_4$	3.5	3.8	2.6	2.8

S.VI. OPTICAL BAND GAPS

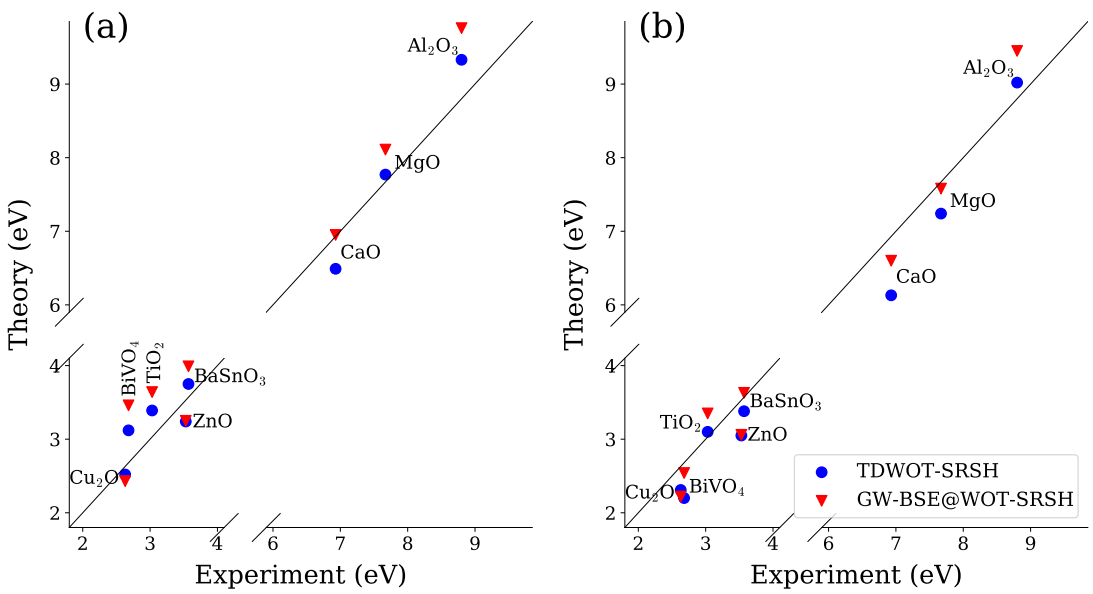

FIG. S.III: Optical band gaps from TDWOT-SRSH and G_0W_0-BSE@WOT-SRSH, shown as both (a) uncorrected and (b) corrected for vibrational renormalization effects, compared with experimental values as reported in the main text. The straight line indicates perfect agreement.

[1] G. Kresse and J. Furthmüller, Phys. Rev. B **54**, 11169 (1996).
[2] G. Kresse and D. Joubert, Phys. Rev. B **59**, 1758 (1999).
[3] G. Makov and M. C. Payne, Phys. Rev. B **51**, 4014 (1995).
[4] M. Leslie and N. J. Gillan, J. Phys. C: Solid State Phys. **18**, 973 (1985).
[5] H.-P. Komsa, T. T. Rantala, and A. Pasquarello, Phys. Rev. B **86**, 045112 (2012).
[6] R. Rurali and X. Cartoixá , Nano Lett. **9**, 975 (2009).

[7] A. A. Mostofi, J. R. Yates, G. Pizzi, Y.-S. Lee, I. Souza, D. Vanderbilt, and N. Marzari, Comput. Phys. Commun. **185**, 2309 (2014).

[8] D. Wing, J. B. Haber, R. Noff, B. Barker, D. A. Egger, A. Ramasubramaniam, S. G. Louie, J. B. Neaton, and L. Kronik, Phys. Rev. Mater. **3**, 064603 (2019).

[9] P. Giannozzi, S. Baroni, N. Bonini, M. Calandra, R. Car, C. Cavazzoni, D. Ceresoli, G. L. Chiarotti, M. Cococcioni, I. Dabo, *et al.*, J. Phys.: Condens. Matter **21**, 395502 (2009).

[10] P. Giannozzi, O. Andreussi, T. Brumme, O. Bunau, M. Buongiorno Nardelli, M. Calandra, R. Car, C. Cavazzoni, D. Ceresoli, M. Cococcioni, *et al.*, J. Phys.: Condens. Matter **29**, 465901 (2017).

[11] P. Giannozzi, O. Baseggio, P. Bonfà, D. Brunato, R. Car, I. Carnimeo, C. Cavazzoni, S. de Gironcoli, P. Delugas, F. Ferrari Ruffino, *et al.*, J. Chem. Phys. **152**, 154105 (2020).

[12] J. Deslippe, G. Samsonidze, D. A. Strubbe, M. Jain, M. L. Cohen, and S. G. Louie, Comput. Phys. Commun. **183**, 1269 (2012).

[13] D. R. Hamann, Phys. Rev. B **88**, 085117 (2013).

[14] M. van Setten, M. Giantomassi, E. Bousquet, M. Verstraete, D. Hamann, X. Gonze, and G.-M. Rignanese, Comput. Phys. Commun. **226**, 39 (2018).

[15] M. Rohlfing, P. Krüger, and J. Pollmann, Phys. Rev. Lett. **75**, 3489 (1995).

[16] W. Luo, S. Ismail-Beigi, M. L. Cohen, and S. G. Louie, Phys. Rev. B **66**, 195215 (2002).

[17] M. L. Tiago, S. Ismail-Beigi, and S. G. Louie, Phys. Rev. B **69**, 125212 (2004).

[18] A. Fleszar and W. Hanke, Phys. Rev. B **71**, 045207 (2005).

[19] S. L. Adler, Phys. Rev. **126**, 413 (1962).

[20] N. Wiser, Phys. Rev. **129**, 62 (1963).

[21] M. Del Ben, F. H. da Jornada, G. Antonius, T. Rangel, S. G. Louie, J. Deslippe, and A. Canning, Phys. Rev. B **99**, 125128 (2019).

[22] R. W. Godby and R. J. Needs, Phys. Rev. Lett. **62**, 1169 (1989).

[23] A. Oschlies, R. W. Godby, and R. J. Needs, Phys. Rev. B **51**, 1527 (1995).

[24] P. Larson, M. Dvorak, and Z. Wu, Phys. Rev. B **88**, 125205 (2013).

[25] J. Deslippe, G. Samsonidze, M. Jain, M. L. Cohen, and S. G. Louie, Phys. Rev. B **87**, 165124 (2013).

[26] S. Lany, Phys. Rev. B **87**, 085112 (2013).

[27] F. Bruneval, *Exchange and Correlation in the Electronic Structure of Solids, from Silicon to Cuprous Oxide: GW Approximation and Beyond*, Ph.D. thesis, Ecole Polytechnique (2005).

[28] J. P. Perdew and A. Zunger, Physical Review B **23**, 5048 (1981).

[29] M. R. Filip, J. B. Haber, and J. B. Neaton, Phys. Rev. Lett. **127**, 067401 (2021).